Efficiency of band edge optical transitions of two-dimensional monolayer materials: A high-throughput computational study

A. F. Gómez-Bastidas ⊙,[1,*] Karthik Sriram ⊙,[1,2] A. C. Garcia-Castro ⊙,[3] and Oleg Rubel ⊙[1,†]

[1]*Department of Materials Science and Engineering, McMaster University, 1280 Main Street West, Hamilton, Ontario L8S 4L8, Canada*
[2]*Department of Metallurgical and Materials Engineering, Indian Institute of Technology Madras, Chennai 600036, India*
[3]*School of Physics, Universidad Industrial de Santander, Carrera 27 Calle 9, Bucaramanga SAN-680002, Colombia*

We performed high-throughput density functional theory calculations of optical matrix elements between band edges across a diverse set of nonmagnetic two-dimensional monolayers with direct band gaps. Materials were ranked as potential optical emitters, leading to the identification of transition-metal nitrogen halides (ZrNCl, TiNBr, TiNCl) and bismuth chalcohalides (BiTeCl) with optical coupling strengths comparable to or exceeding that of MoS_2. Despite strong in-plane dipole transitions, most two-dimensional materials underperform relative to bulk semiconductors due to a combination of factors, including the absence of out-of-plane optical components, reduced orbital degeneracy at the band edges due to lower crystal symmetry, and spin degeneracy lifting at non-time-reversal-invariant k points. To elucidate the nature of interband transitions, we introduced the orbital overlap tensor and established a correlation between anomalous Born effective charges and optical coupling, linking charge redistribution to transition strength. We also identified chalcogen-mediated d-d transitions as a key mechanism enabling strong optical responses in transition-metal dichalcogenides. An analytical model for the radiative recombination coefficient, incorporating multivalley effects, was derived and benchmarked against full first-principles calculations. Excitonic corrections were found to be essential for quantitative agreement with experiment. Notably, some direct-gap monolayers host dark excitons as their lowest-energy excitonic states, rendering them quasidirect band gap semiconductors and underscoring the importance of excitonic effects for tuning light emission properties in two-dimensional materials.

I. INTRODUCTION

The emergence of two-dimensional monolayer materials (2DMs) as physically realizable systems has resulted in one of the most active fields in modern materials research [1–3]. Atomically thin materials provide an ideal platform for investigating electronic properties under quantum confinement, particularly the enhancement of excitonic effects [1–4]. Reducing layered materials to a single sheet opens up possibilities for modifying the optoelectronic properties of these materials, such as band gap engineering [5]. Furthermore, the transition from a bulk material to a two-dimensional monolayer can lead to a crossover from an electronic indirect band gap to a direct band gap material, which is promising for light-emitting applications. Prominent examples of materials that exhibit this modification of band type include members of the transition metal dichalcogenides (TMDCs) family [6,7], tellurene [8], and phosphorene (black phosphorus) [9–11]. Among the TMDC family, the monolayer of molybdenum disulfide MoS_2 has been extensively studied, and its electronic properties have been predicted through *ab initio* simulations and confirmed by experiments [6,12–14]. This 2D direct band gap semiconductor material exhibits strong light emission through luminescence [15,16], high light absorption [17],

strongly bound exciton peaks [6], and circular dichroism [18,19]. As a result, there is a growing interest in studying the optical properties of 2D direct band gap materials [20–26].

While the presence of a direct band gap is a necessary condition for efficient optical emitters, it is insufficient on its own. In solid-state systems, under the assumption of the electric dipole approximation, the inter-band optical matrix elements for unpolarized light are directly proportional to the linear momentum matrix elements, denoted as $\boldsymbol{p}_{vc,\boldsymbol{k}} = \langle \phi_{c,\boldsymbol{k}} | \hat{\boldsymbol{p}} | \phi_{v,\boldsymbol{k}} \rangle$. Here, $\hat{\boldsymbol{p}}$ represents the momentum operator, $\boldsymbol{k}$ is a wave vector within the Brillouin zone (BZ), and $|\phi_{v,\boldsymbol{k}}\rangle$ and $|\phi_{c,\boldsymbol{k}}\rangle$ denote Bloch states in the occupied valence band and the unoccupied conduction band, respectively (see Refs. [[27], chap. 3] and [[28], chap. 9]). The momentum matrix elements play a crucial role in studying the absorption and emission characteristics of direct gap semiconductors [29–32], as they are essential for the computation of the optical absorption coefficient, radiative lifetime, and luminescence intensity [[27], chap. 3 and 4]. For bulk group-IV, III-V, and II-VI semiconductors, the momentum matrix elements are often expressed in energy units [[33], p. 71]

$$E_P = \frac{2\langle p_{vc_1}^2 \rangle_\alpha}{m_0}, \qquad (1)$$

where m_0 is the rest mass of an electron and $\langle p_{vc_1}^2 \rangle_\alpha = (p_{x,vc_1}^2 + p_{y,vc_1}^2 + p_{z,vc_1}^2)/3$ is the average matrix element over Cartesian directions $\alpha = x, y, z$ to account for an arbitrary

*Contact author: gomezbaa@mcmaster.ca
†Contact author: rubelo@mcmaster.ca

195426-1

polarization of light. Here, p_{vc_1} includes coupling between the heavy-hole, light-hole, split-off bands, and only *one* of the double-degenerate conduction band edge (CBE) states at Γ point. The optical coupling between the band edges in these traditional optoelectronic materials typically falls in the range of $E_P = 14$–31.4 eV, exhibiting low sensitivity to chemical composition [26,34–37]. It is intriguing to compare this characteristic to the optical coupling in 2DMs.

A substantial body of optical calculations related to 2DMs has been conducted, focusing on properties such as absorption spectra and interband polarizability [4,6,14,38–44]. However, the results of these calculations are not directly correlated with the efficiency of these materials as optical emitters, which requires knowledge of the optical coupling strength at the band edges. For instance, one of key findings in Ref. [39] was that materials such as T-PtTe$_2$, H-TiS$_2$, and T-SnSe$_2$ exhibit the highest absorbance in the near-infrared and ultraviolet ranges. However, these materials all possess an indirect band gap, making them unsuitable for strong spontaneous light emission. This example underscores why absorbance far from the band edge may be insufficient to identify strong light-emitting materials.

The momentum or velocity matrix elements at the band edge of monolayer MoS$_2$, as reported in Ref. [45], allow evaluation of the in-plane optical coupling parameter $E_P =$ 4.1–5.8 eV ($\alpha = x, y$) at the K point of the hexagonal 2D BZ. This range reflects differences between exchange-correlation approximations. Accordingly, the value of E_P in one of the most studied 2DMs (MoS$_2$) is lower by approximately a factor of four compared to well-established bulk semiconductors known for efficient radiative recombination. However, the origin of this underperformance remains unclear, and it is not known whether this trend is typical among other 2DMs, as comparable matrix elements have not been widely reported in the literature.

The present study aims to fill this gap by investigating the momentum matrix elements of 2DMs using density functional theory (DFT) [46,47] within a high-throughput framework. Structural data for the 2DMs were sourced from the computational 2D materials database (C2DB) [42,48]. Our focus specifically encompassed thermodynamically and dynamically stable, nonmagnetic, direct band gap semiconductors. Of the 15 733 materials in the database, we filtered the data according to the constraints explained in Sec. II, ultimately calculating the momentum matrix elements between the valence band edge (VBE) and CBE for 358 monolayers. We determined the orbital character of VBE and CBE states and categorized the materials based on the proportions of $s \rightarrow p$, $p \rightarrow d$, and forbidden ($\Delta \ell \neq \pm 1$) transitions. Counterintuitively, TMDCs predominantly exhibited forbidden (mainly $d \rightarrow d$) transitions, despite demonstrating significant optical activity. We attribute this observation to a high polarizability of transition metal nonbonding d states. This phenomenon is observed in conjunction with a dynamic charge transfer and was first recognized by Pike *et al.* [49] in the context of anomalous Born effective charges (BECs) in hexagonal TMDCs. We compared strength of the optical coupling at the band edges of the 2DMs to those of conventional optoelectronic bulk semiconductors. To illustrate practical implications of momentum matrix elements at the band edges,

we computed the radiative recombination coefficient B_{2D} and the radiative lifetime, which is an experimentally accessible physical quantity. These parameters are critical for optoelectronic applications such as light-emitting diodes, lasers, and photosensors.

II. COMPUTATIONAL DETAILS

The crystal structures utilized in this investigation were obtained from the C2DB database [42]. Two-dimensional semiconductors exhibiting direct electronic band gaps of up to 3.5 eV were selected based on their dynamic and thermodynamic stability. The selection criteria required nonimaginary frequencies in the phonon dispersion and energy values above the convex hull of less than 50 meV per atom. For the most promising materials (high $\langle p_{vc,k_0}^2 \rangle_{\alpha,T}$), discussed in this text, we conducted additional assessments of their viability by identifying a parent two-dimensional bulk structure that has been either experimentally reported or listed as stable in the Materials Project database [50,51].

The DFT [46,47] based calculations were conducted using the Vienna *ab initio* simulation VASP package [52,53] (version 6.4.0), which employs the projector augmented wave pseudopotential method for the basis set treatment [54]. The Perdew-Burke-Ernzerhof (PBE) exchange-correlation functional was employed [55]. The cutoff energy for the plane wave expansion was set to the maximum ENMAX parameter (POTCAR file) from the atomic species in the compounds. Projector augmented-wave pseudopotentials [56] (version 5.4) were employed. The number of valence electrons and cutoff energy for each element can be found in Table S1 from Ref. [57]. A Γ-centered unshifted k mesh was utilized. We employed the fully automatic generation scheme with a $R_k = 20$ parameter, which determines the number of subdivisions for every reciprocal lattice vector $\boldsymbol{b}_i$ as $N_i =$ int[max$(1, R_k|\boldsymbol{b}_i| + 0.5)$]. In cases where the k point corresponding to the band edges was not included in the automatic mesh, it was explicitly added to the list with a weight of zero for the computation of the momentum matrix elements. The precision mode (PREC flag) was set to "accurate." This resulted in a denser Fourier grid for charge densities and potentials. Spin-orbit coupling (SOC) was considered in all calculations [58]. The convergence criteria for the total energy in the electronic self-consistent field loop was set at 10^{-6} eV. For the orbital partial occupancies, we used a 0.01 eV Gaussian smearing width.

The momentum matrix elements were transformed from the dipole matrix elements $\boldsymbol{r}_{vc,k}$, read from VASP WAVEDER file, as

$$\boldsymbol{p}_{vc,k} = \frac{\mathbb{i} m_0}{\hbar}(E_{c,k} - E_{v,k})\boldsymbol{r}_{vc,k}, \qquad (2)$$

where $\mathbb{i}$ is the imaginary unit, $\hbar$ is the reduced Planck constant, and $E_{v/c,k}$ are DFT energy eigenvalues of states in the valence/conduction band. Convergence tests for the absolute square momentum matrix elements were performed on three representative materials with respect to R_k, cutoff energy, and precision mode computational parameters. Results of the tests are presented in Fig. S1 [57]. It is noteworthy that both the oscillator strength and the dipole matrix elements are influenced

by the band gap value via the term $E_{c,\boldsymbol{k}} - E_{v,\boldsymbol{k}}$ in Eq. (2). However, accurately determining the band gap in standard DFT calculations can be problematic, making it challenging to compare values of the oscillator strength and of the dipole matrix elements at the band edge between different materials. On the other hand, $\boldsymbol{p}_{vc,\boldsymbol{k}}$ is not affected by the band gap error, providing a more suitable metric for comparing materials [59], [[60], App. A].

The site- and orbital-projected wave-function characters, resolved into s, p, and d contributions, were calculated using VASP [61]. These projections were extracted from the PROCAR file, which contains the decomposition of Kohn-Sham wave functions onto atomic-like orbitals at each k point in the BZ.

Effective charges (Bader and Born) were sourced from the C2DB database [42,48]. For instances without reported Bader charabsolute squareges, we calculated them and verified their convergence (Tables S2 and S3 [57]). The cell-periodic part of pseudo-wavefunctions $\tilde{u}_{\boldsymbol{k}}(\boldsymbol{r})$ was extracted using VASPKIT [62] to visualize the overlap $\tilde{u}_{\boldsymbol{k}}^*(\boldsymbol{r})\tilde{u}_{\boldsymbol{k}+\boldsymbol{q}_\alpha}(\boldsymbol{r})$ in real space with a small shift q of the magnitude approximately 0.004 Å^{-1}. The bimolecular radiative recombination coefficients were computed at the DFT level by adapting the methodology outlined by Xu *et al.* [63] to 2DMs. The k meshes employed for the calculation included at least a hundred times more k points for the irreducible BZ sampling than those employed for the momentum matrix elements calculation.

Excitonic properties of selected 2DMs were calculated using VASP's implementation of the Bethe-Salpeter equation (BSE) [64] with the Tamm-Dancoff approximation. SOC was included for all materials. Preliminary ground state calculations, virtual orbital calculations, and derivatives of the orbitals with respect to the Bloch vectors were performed at the PBE level. Γ-centered k mesh with 32 divisors per Å^{-1} length of reciprocal lattice vectors is used to sample the BZ. Quasiparticle energies and the screened Coulomb kernel were obtained from a subsequent G_0W_0 calculation. At least 16 occupied and 16 unoccupied orbitals near the band edges were included in the BSE calculation. Sample input files are available from a Zenodo repository [65].

III. RESULTS AND DISCUSSION

A. Momentum matrix elements

As an initial step, we have computed the momentum matrix elements $\boldsymbol{p}_{vc,\boldsymbol{k}}$ between states at the band edges based on the electronic structure of 2DMs. These matrix elements are essential for understanding optical emission resulting from the recombination of charge carriers between CBE and VBE. Our study specifically focuses on direct band gap 2DMs. Generally, there may exist a group of bands $v_j \in \{v_1, v_2, \ldots\}$ and $c_i \in \{c_1, c_2, \ldots\}$ close to the band edge at $\boldsymbol{k}_0$ as illustrated in Fig. 1. These bands may either be degenerate, as in the case of monolayer ReS$_2$, or the degeneracies may be lifted, for example, due to spin-orbit coupling (SOC) as seen in monolayer MoS$_2$. The effective optical matrix element for spontaneous emission is obtained by summing over all possible pairs $v_j c_i$ as follows:

$$\langle p_{vc,\boldsymbol{k}_0}^2 \rangle_{\alpha,T} = \sum_{i,j} \langle p_{v_j c_i,\boldsymbol{k}_0}^2 \rangle_\alpha \exp\left[-(\Delta_{c_i} + \Delta_{v_j})/k_{\mathrm{B}}T\right], \quad (3)$$
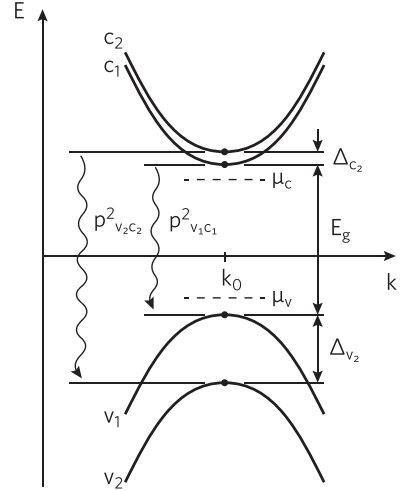

FIG. 1. Schematic band structure with nondegenerate bands showing two optically active transitions from a total of four possible ones at the $\boldsymbol{k}_0$ valley. Band splittings Δ_{c_i} and Δ_{v_j} are positively defined and are measured relative to the band edges.

where Δ_{c_i} and Δ_{v_j} are positively defined band splittings measured relative to the band edges (Fig. 1). The exponential term represents the probability of occupancy of energy levels above the band gap, under the assumption of a dilute limit for the charge carrier density. For instance, the lowest energy transition A dominates the photoluminescence spectrum of monolayer MoS$_2$ at room temperature [66] in contrast to the second lowest energy transition B with an excess energy of $\Delta_{c_2} + \Delta_{v_2} \approx 0.15$ eV, which exhibits a considerably lower spectral intensity. Although the matrix elements $p_{v_1 c_1,K}^2$ and $p_{v_2 c_2,K}^2$ possess identical magnitudes, the contribution of the second transition to radiative recombination at room temperature is significantly reduced owing to $\Delta_{c_2} + \Delta_{v_2} \gg k_{\mathrm{B}}T$.

Figure 2 presents ranking of 2DMs according to the magnitude of momentum matrix elements computed using Eq. (3) and truncated at $\langle p_{vc,\boldsymbol{k}_0}^2 \rangle_{\alpha,300\,\mathrm{K}} = 0.01$ a.u. The optical activity of most TMDCs is ranked as above average. The following prominent 2DMs, that have been previously synthesized, are labeled in Fig. 2: MoS$_2$ [12,16,67,68], MoSeS [69], MoSe$_2$ and WSe$_2$ [70], MoTe$_2$ [71], ReS$_2$ [72], and WS$_2$ [73]. The top ranked monolayer materials in Fig. 2 (not explicitly labeled) are derived from naturally occurring bulk layered phases, suggesting that exfoliation is plausible. Materials with the highest optical coupling between band edges are listed in Table I along with well-established TMDCs. The optical coupling strength of the non-TMDCs materials is comparable and even superior to that of TMDCs, indicating potential for optoelectronic applications. Some of those materials have the band gap at the Heyd-Scuseria-Ernzerhof (HSE06) level, including SOC, within the visible range of the electromagnetic spectrum (1.8–3.1 eV). The direct transition occurs at Γ point in the BZ for all the non-TMDCs and at $K = (1/3, 1/3, 0)$ for the TMDCs.

The dashed lines in Fig. 2 represent the optical matrix elements for selected bulk semiconductors. The momentum matrix elements $\langle p_{v_j c_i,\boldsymbol{k}_0}^2 \rangle_\alpha$ for individual transitions were extracted from Ref. [45] at the DFT-PBE level and incorporated into Eq. (3) to compute the effective optical matrix elements
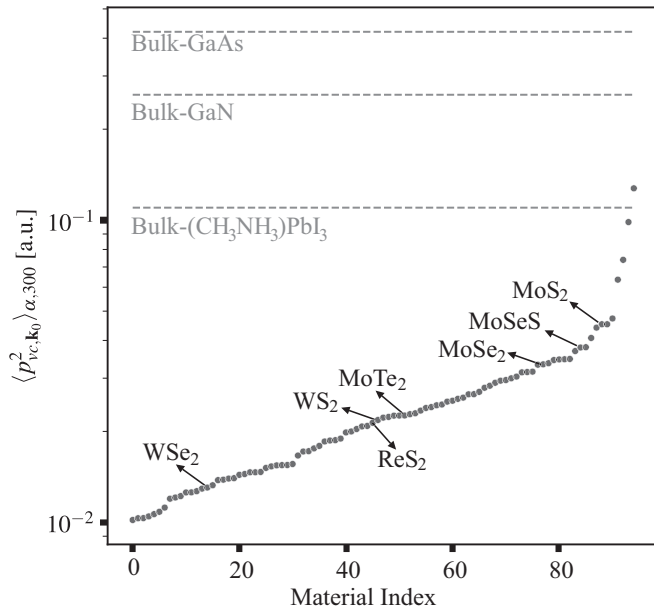
FIG. 2. Ranking of direct band gap 2DMs according to their optical activity captured by the polarization-average momentum matrix element at the band edges $\langle p_{vc}^2 \rangle_{\alpha,300\,\text{K}}$ (in atomic units) defined by Eq. (3). Only materials with the highest optical activity are presented and arranged in ascending order. The dashed lines mark values corresponding to the well-known optically active bulk semiconductors.

of $p_{z,v_j c_i}^2$ components. Degeneracies at the band edges also play an important role. Traditional group III-V semiconductors with the zinc-blende structure and sp^3 bonding, such as GaAs, exhibit a twofold degeneracy at the valence band edge (excluding spin), which arises from the cubic symmetry of the crystal. This degeneracy provides additional pathways for optical transitions, resulting in enhanced dipole matrix elements. In contrast, wurtzite GaN does not exhibit light- and heavy-hole degeneracy at the valence band edge due to crystal-field splitting. Nonetheless, it remains a highly efficient light emitter, as the splitting is relatively small and does not significantly suppress radiative transitions.

In contrast, the top-performing 2DMs shown in Fig. 2 typically exhibit no orbital degeneracy at the band edges due to reduced symmetry. As a result, the number of available optical transitions is lower, leading to reduced overall optical coupling compared to bulk semiconductors. Additionally, when the direct transition occurs at a non-time-reversal-invariant k-point, spin degeneracy is lifted by spin-orbit coupling, leaving even fewer symmetry-allowed pathways for optical transitions. In hexagonal TMDCs, this lifting of spin degeneracy directly results in spin-forbidden transitions, such as the $K_{v_1} - K_{c_2}$ transition, and leads to the underpopulation of the v_2 band due to the large spin-orbit splitting Δ_{so} [14,77,78]. These symmetry- and spin-related effects help explain the comparatively weaker optical coupling observed in 2DM relative to bulk semiconductors.

B. Orbital character of band edges and TMDCs anomaly

Analysis of the orbital composition of states involved in radiative transitions will provide insight into the factors influencing the strength variability of optical transitions. Vectors of orbital characters associated with states in the vicinity of VBE and CBE are expressed as

$$\boldsymbol{v} = (s_v, p_v, d_v) = \left(\sum_j s_{v_j} \exp[-\Delta_{v_j}/k_B T], \sum_j p_{v_j} \exp[-\Delta_{v_j}/k_B T], \sum_j d_{v_j} \exp[-\Delta_{v_j}/k_B T] \right), \tag{4a}$$

$$\boldsymbol{c} = (s_c, p_c, d_c) = \left(\sum_i s_{c_i} \exp[-\Delta_{c_i}/k_B T], \sum_i p_{c_i} \exp[-\Delta_{c_i}/k_B T], \sum_i d_{c_i} \exp[-\Delta_{c_i}/k_B T] \right) \tag{4b}$$

with the summation indices i and j running over a set of conduction and valence bands, respectively. Symbols s, p, and d represent the projected wavefunction character of each orbital, summed over all atomic sites (not to be confused with the notation for the momentum matrix elements, p_{vc}). The orbital characters of individual bands are weighted by the exponential factor (see schematic Fig. 1) to account for their occupancy at the finite temperature. Building upon the general idea of Woods-Robinson *et al.* [79], we define a new metric (tensor) to characterize the orbital overlap between VBE and CBE states

$$\boldsymbol{P}' = \boldsymbol{v} \otimes \boldsymbol{c} = \begin{pmatrix} s_v s_c & s_v p_c & s_v d_c \\ p_v s_c & p_v p_c & p_v d_c \\ d_v s_c & d_v p_c & d_v d_c \end{pmatrix}. \tag{5}$$

The matrix is normalized as

$$\boldsymbol{P} = \boldsymbol{P}' \left(\sum_{n,m=1}^{3} P'_{nm} \right)^{-1}, \tag{6}$$

resulting in $\sum_{n,m=1}^{3} P_{nm} = 1$. Elements of the tensor can be assigned to transitions between orbitals as

$$P_{s \to p} = P_{12} + P_{21}, \quad \text{(allowed)} \tag{7a}$$

$$P_{p \to d} = P_{23} + P_{32}, \quad \text{(allowed)} \tag{7b}$$

$$P_{\times} = P_{11} + P_{22} + P_{33} + P_{13} + P_{31}. \quad \text{(forbidden)} \tag{7c}$$

between band edges. Comparing optical coupling strengths reveals that the best-performing 2DMs fall short of established bulk optoelectronic materials. The reduced optical performance of 2DMs is partly due to the lack of optical coupling with out-of-plane light polarization in most monolayer materials. Particularly, the absence of out-of-plane mirror symmetry is a necessary but not sufficient condition for the existence

TABLE I. Characteristics of direct band gap 2DMs having strongest optical coupling at the band edges. The band gap E_g and BSE exciton energies E_{exc} include SOC. The superscript $(^{\times n})$ reflects the degeneracy of exciton states.

Material	E_g (eV)[a]	k_0	$\langle p^2_{vc,k_0}\rangle_{\alpha,300\,K}$ (a.u.)	$E^{(\lambda)}_{exc}$ (eV)	$\langle p^2_{exc}(\lambda)\rangle_\alpha$ (a.u.)	C2DB id	Parent bulk structure[b]
GaSeCl	3.6	Γ	0.13	3.60	0	2ClGaSe-1	[74], mp-1120728
				3.61	0.01		
				3.61	0		
				3.66	0.59		
BiTeCl	1.2	Γ	0.10	$1.33^{\times 2}$	$0.049^{\times 2}$	1BiClTe-1	mp-28944
				$1.34^{\times 2}$	$0.016^{\times 2}$		
Bi_2Se_2Te	0.76	Γ	0.074	$0.70^{\times 4}$	$0^{\times 2}$	1TeBi2Se2-1	sd_1727317
					$0.039^{\times 2}$		cod $-$ 9004849
ZrNCl	3.1	Γ	0.064	$2.50^{\times 3}$	$0^{\times 3}$	2ClNZr-2	sd_1704456
				2.51	0.13		
TiNBr	2.1	Γ	0.047	$1.34^{\times 4}$	$0^{\times 3}$	2BrNTi-1	sd_1704458
					0.053		
MoS_2	2.1	K	0.045	$1.96^{\times 4}$	$0^{\times 2}$	1MoS2-1	sd_0309036
					$0.073^{\times 2}$		
TiNCl	2.1	Γ	0.044	$1.37^{\times 4}$	$0^{\times 3}$	2ClNTi-1	sd_1704459
					0.052		
HgI_2	2.5	Γ	0.041	2.51	0	4HgI2-1	cod-9008155
				2.52	0		
				$2.57^{\times 2}$	0		
				2.62	0		
				$2.67^{\times 2}$	$0.13^{\times 2}$		
MoSeS	1.9	K	0.038	$1.82^{\times 4}$	$0.067^{\times 2}$	1MoSSe-1	[69], mp-1221404
					$0^{\times 2}$		
$MoSe_2$	1.8	K	0.033	$1.67^{\times 2}$	$0.060^{\times 2}$	1MoSe2-1	sd_0309034
				$1.68^{\times 2}$	$0^{\times 2}$		
$Mg_2Al_2Se_5$	2.0	Γ	0.013	$2.13^{\times 2}$	$0^{\times 2}$	1Al2Mg2Se5-1	mp-29624
				$2.14^{\times 2}$	$0.011^{\times 2}$		
GaAs (bulk)	1.3	Γ	0.42	$1.34^{\times 5}$	$0^{\times 5}$	–	–
				$1.34^{\times 3}$	$0.15^{\times 3}$	–	–

[a]Data from C2DB calculated at the Heyd-Scuseria-Ernzerhof'06 screened hybrid functional [75] level including SOC.
[b]The prefix in structures id's corresponds to the following databases: 'mp' Materials Project [50,51], 'cod' Crystallography Open Database [76], 'sd' Springer Materials.

The interpretation of transitions is based on (partial) orbital selection rules in atomic dipolar transitions [[80], chap. 4.3], which is a distant analogy to solids with dispersive bands.

Figure 3 presents a ternary diagram in which all 2DMs are positioned according to the fraction of allowed ($s \to p$, $p \to d$) and forbidden overlaps. Notably, there exists a considerable number of materials that exhibit relatively high optical coupling at the band edges alongside a significant weight of forbidden transitions. TMDCs are among those materials that demonstrate a high fraction of $d \to d$ transitions. In TMDCs, such as MoS_2, the electronic band edges are predominantly composed of d orbitals of the Mo atom, with a small contribution from the p-orbitals of sulfur. Specifically, in the valence band at the $K = (1/3, 1/3, 0)$ point, Mo: $d_{x^2-y^2}$ and d_{xy} orbitals are present, along with a small contribution from the sulfur p_x and p_y orbitals. In the conduction band at the K point, the dominant contribution comes from the Mo d_{z^2} orbital, which is consistent with prior findings [81,82]. According to atomic selection rules, this orbital composition is not expected to result in significant optical coupling. In contrast, hexagonal TMDCs exhibit some of the strongest matrix elements among 2DMs (Fig. 2).
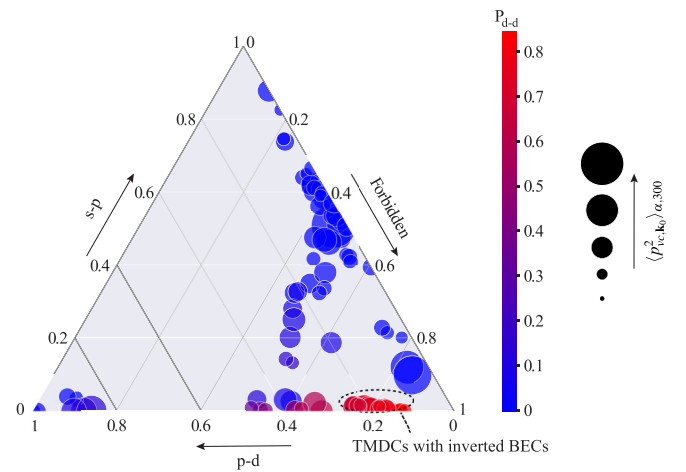

FIG. 3. Orbital overlap ternary diagram where each 2DM from Fig. 2 is presented according to the fraction of allowed ($s \to p$, $p \to d$) and forbidden overlaps at the band edges, as defined by Eq. (7) at room temperature. The size of the markers is proportional to the effective momentum matrix element at the band edges $\langle p^2_{vc}\rangle_{\alpha,300\,K}$ defined by Eq. (3). The color refers to the fraction of $d \to d$ orbital overlap P_{33}.
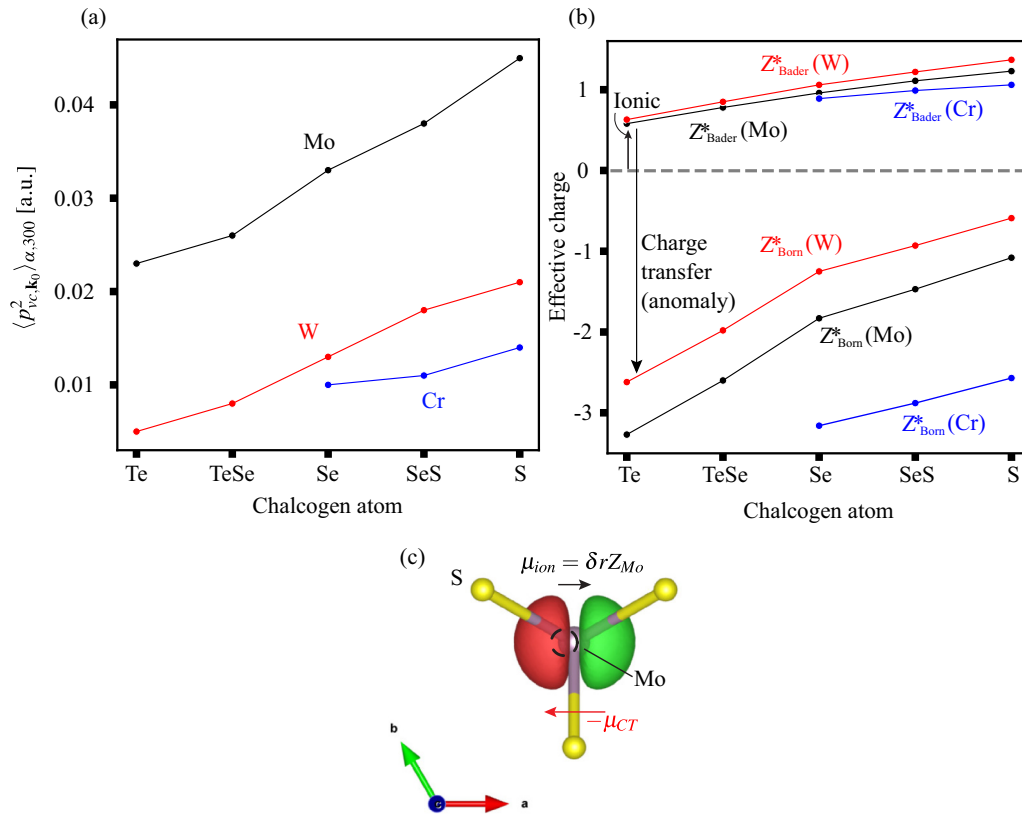
FIG. 4. (a) Momentum matrix elements $\langle p_{vc}^2 \rangle_{\alpha,300\ \mathrm{K}}$ and (b) effective charges of the TM atom plotted as a function of the chalcogen element in group-VI hexagonal TMDCs. The dynamical charge information is represented by the average of the Z_{xx}^A and Z_{yy}^A in-plane components of the Born effective charge tensor. The lines serve as visual aids. (c) Competing dipole moments contributing to the dynamic charge of Mo (see text for details). The local charge transfer (red for charge augmentation and green for charge depletion) gives rise to anomalous BECs.

Two explanations for the observed interband optical coupling in TMDCs have been proposed in the literature. The first proposed explanation pertains to SOC, which is believed to facilitate the dipole transitions [26,40]. However, our calculations of MoS_2, conducted without considering SOC, indicated its effect on the optical matrix elements to be negligible. The second proposed explanation is the trigonal-prismatic crystal field splitting of Mo d states [83]. To test this idea, we performed a DFT calculation of an isolated Mo atom in the trigonal-prismatic coordination of six S atoms in vacuum. The results confirmed the crystal field splitting for the d-electronic levels of Mo, with a lower energy level A_1' composed of d_{z^2} followed by two degenerate energy levels E' composed of $d_{x^2-y^2}$ and d_{xy}, and a twofold degenerate higher energy levels E'' composed of d_{xz} and d_{yz}. However, no optical coupling between E' and A_1' states was observed contrary to the claims in Ref. [83].

To elucidate the efficiency of optical coupling at the band edge, we analyzed chemical trends within the family of group-VI TMDCs, specifically MX_2 (space group No. 187) and MZX (space group No. 156), where M represents Mo, W, or Cr, and X and Z denote S, Se, or Te. The optical coupling values exhibit an increase in materials with more electronegative chalcogen atoms, as illustrated in Fig. 4(a). To further investigate this chemical trend, we examined the Bader charges, which estimate charge transfer and reveal electron

density redistribution due to bonding. Consequently, they are often used to infer the oxidation states of elements in solids. The values for the Bader charges depicted in Fig. 4(b) indicate that electrons transfer from the transition metal (TM) to the chalcogen atom, suggesting an ionic character of bonding. This observed trend deviates from the conventional understanding in the literature, where enhanced overlap between band edge states (orbital hybridization), rather than electron transfer, is considered the driving mechanism for increased optical coupling [32,84–87].

We analyze the electronic charge redistribution in response to atomic displacements, which manifests as induced macroscopic polarization and is captured by the BECs [88], to further clarify the counterintuitive correlation between bonding mechanisms and optical coupling. The BECs characterize the dynamical behavior of charge and take into account contribution from both ionic charge and electron density redistribution in response to the perturbation [88]. They have been extensively employed in the study of ferroelectric materials [89]. It has been established that the presence of BEC magnitudes that significantly deviate from nominal ionic charges is attributed to dynamical contributions, which arise from two charge redistribution mechanisms. The first mechanism involves the delocalized transfer of electrons or interatomic hybridization, while the second mechanism pertains to on-site changes in hybridization or local

displacements of the electronic cloud relative to the atom [89].

In the case of the examined TMDCs monolayers, the Bader static and Born dynamic charges exhibit opposite sign [Fig. 4(b)]. The entire set of monolayers with inverted charges are circled in Fig. 3. This phenomenon was explained by Pike et al. [49], who found that an applied external electric field induces electron density changes predominantly localized around Mo atoms, exhibiting a hybridized d-orbital configuration. In contrast, the alteration in electron density surrounding S atoms is negligible. These nonbonding states, located at the top of the valence band, are sensitive to displacements of the Mo atoms, leading to local changes in polarization near the Mo sites [Fig. 4(c)]. The dipole μ_{CT} resulting from the charge transfer near Mo atom counteracts the ionic component $\delta r Z_{Mo}$. This phenomenon governs the sign inversion of BECs in hexagonal TMDCs [49]. This behavior establishes a heuristic link between anomalous BECs and interband optical transitions. Consequently, the high optical coupling in TMDCs can be linked to the high polarizability of TM d-states particularly at the band edge. The chalcogen p orbitals mediate interaction between TM d orbitals without directly contributing to the band edge states.

To demonstrate that the optical activity in TMDCs is localized around the TM sites for transitions between band edges, we use the correspondence between velocity and momentum matrix elements, $p = m_0 v$. This relation is valid for local potentials [90], such as PBE in DFT. The velocity matrix element can be expressed in terms of an overlap matrix element between two states with a small finite displacement q in reciprocal space [31,45,91]

$$v_{\alpha,vc}(\mathbf{k}) = \lim_{q \to 0} (\hbar q)^{-1} \langle u_{c,\mathbf{k}+\mathbf{q}_\alpha} | u_{v,\mathbf{k}} \rangle [E_c(\mathbf{k}+\mathbf{q}_\alpha) - E_v(\mathbf{k})],$$

$$(8)$$

where $u_{v/c,\mathbf{k}}(\mathbf{r})$ represents the cell-periodic part of the Bloch function for a state in the valence/conduction band. For visualization, we employ the cell-periodic part of the Bloch pseudo-wavefunction $\tilde{u}_{v/c,\mathbf{k}}(\mathbf{r})$ within the projector augmented wave formalism to evaluate the overlap $\tilde{u}^*_{c,\mathbf{k}+\mathbf{q}_\alpha}(\mathbf{r}) \tilde{u}_{v,\mathbf{k}}(\mathbf{r})$, serving as a measure of optical activity in real space. Figure 5(a) illustrates that the optical activity between band edges in monolayer MoS$_2$ is indeed localized near the Mo sites within the Mo plane, with negligible involvement of S atoms. This behavior is strikingly different from materials like GaSeCl (layered group No. 32), where the high optical matrix element arises from the contributions of both Se and Cl atoms [Fig. 5(b)].

C. Radiative recombination coefficient B of selected compounds

Next we will illustrate how optical matrix elements propagate into tangible optical characteristics of 2DMs. The dynamics of radiative recombination of charge carriers within the bulk of an intrinsic semiconductor ($n = p$) is governed by the equation
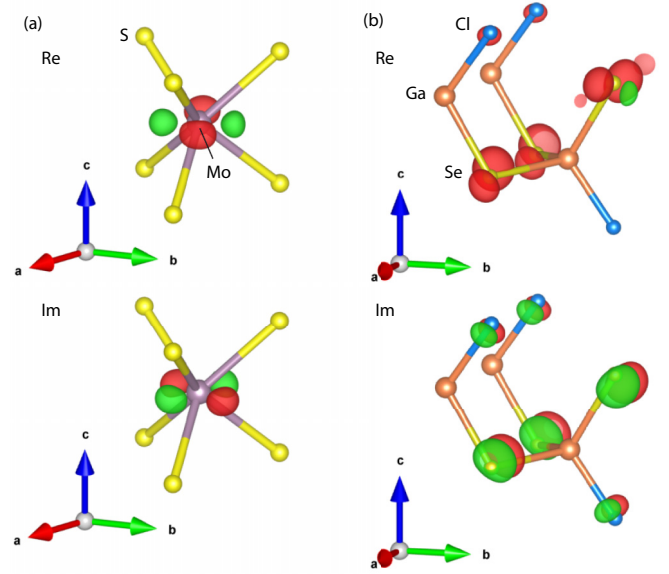
$$\left(\frac{dn}{dt}\right)_{rad} = -Bn^2 \qquad (9)$$

FIG. 5. Real-space overlap $\tilde{u}^*_{v,\mathbf{k}}(\mathbf{r}) \tilde{u}_{c,\mathbf{k}+\mathbf{q}_\alpha}(\mathbf{r})$, representing the interband optical matrix element induced by an electromagnetic field polarized along Cartesian direction α. (a) MoS$_2$ at the K point, direction y. (b) GaSeCl at the Γ point, direction x. Isosurfaces show the real and imaginary parts of the overlap, with red and green indicating positive and negative values, respectively. The phase is chosen such that $\text{Im}[\langle \tilde{u}_{v,\mathbf{k}} | \tilde{u}_{c,\mathbf{k}+\mathbf{q}_\alpha} \rangle] = 0$.

with the bimolecular radiative recombination coefficient expressed as [63,92]

$$B = (2\pi)^{-d} n^{-2} \sum_{i,j} \int_{BZ} f_{c_i,\mathbf{k}} (1 - f_{v_j,\mathbf{k}}) A_{v_j c_i,\mathbf{k}} \, d\mathbf{k}, \qquad (10)$$

where f is the Fermi-Dirac occupation probability, $A_{v_j c_i,\mathbf{k}}$ is the transition rate between states, and d is a dimensionality of the system ($d = 3$ in bulk or $d = 2$ for 2DMs). The integration can also be done over the irreducible BZ by taking into account multiplicity of k points. The transition rate between two states is given by the Einstein coefficient [[27], p. 347]

$$A_{v_j c_i,\mathbf{k}} = \frac{n_r q_e^2}{\pi \epsilon_0 \hbar^2 m_0^2 c^3} \left(E_{c_i,\mathbf{k}} - E_{v_j,\mathbf{k}} \right) \langle p^2_{v_j c_i,\mathbf{k}} \rangle_\alpha, \qquad (11)$$

where n_r is the isotropic refractive index of the solid, e is the elementary charge, ϵ_0 is the permittivity of free space, and c is the speed of light in vacuum. Following mathematical derivations (see Appendix), we obtained the 2D spontaneous recombination coefficient (cm^2/s) for a simple nondegenerate two-band model in the limit of low carrier density

$$B_{2D} = \frac{2q_e^2}{c^3 m_0^2 \epsilon_0 k_B T} \frac{n_r E_g \langle p^2_{vc,\mathbf{k}_0} \rangle_\alpha}{g_{\mathbf{k}_0}(m_c + m_v)}. \qquad (12)$$

Here $\mathbf{k}_0$ denotes the momentum-space location of the valley where direct optical transitions occur in the BZ, and $g_{\mathbf{k}_0}$ is its multiplicity. The final term highlights material-specific parameters, beyond the momentum matrix elements, that influence the rate of radiative recombination. In particular, the

presence of multiple $\boldsymbol{k}_0$ valleys ($g_{\boldsymbol{k}_0} > 1$) as well as heavier effective masses reduce recombination rates by delocalizing carrier density in reciprocal space. Real-world materials often exhibit multiple bands with varying degeneracy near the band edges, as illustrated schematically in Fig. 1, where Δ_{c_i} and Δ_{v_j} represent the energy separations of conduction and valence subbands relative to their respective band edges. Equation (12) can be recast in more general form as

$$B_{2D} = \frac{2q_e^2}{c^3 m_0^2 \epsilon_0 k_B T} \frac{n_r \sum_{i,j}(E_g + \Delta_{c_i} + \Delta_{v_j})\langle p_{v_j c_i, \boldsymbol{k}_0}^2 \rangle_\alpha \exp\left[-(\Delta_{c_i} + \Delta_{v_j})/k_B T\right] m_{c_i} m_{v_j}/(m_{c_i} + m_{v_j})}{g_{\boldsymbol{k}_0}\left[\sum_i m_{c_i} \exp\left(-\Delta_{c_i}/k_B T\right)\right]\left[\sum_j m_{v_j} \exp\left(-\Delta_{v_j}/k_B T\right)\right]} \qquad (13)$$

with the summation indices i and j running over a set of conduction and valence bands, respectively. This expression inherently accounts for band degeneracy.

We evaluate the bimolecular recombination coefficient in MoS_2 in the regime of independent charge carriers (excitonic effects will be discussed later). The average refractive index of $\langle n_r \rangle_\alpha = 3.6$ was estimated from experimental data [93] based on in-plane and out-of-plane values. The effective masses of $m_c = 0.43 m_0$ and $m_v = 0.53 m_0$ are sourced from C2DB. Electronic structure parameters: $E_g = 1.58$ eV, $\Delta_{c_2} = 3$ meV, $\Delta_{v_2} = 150$ meV, $p_{x/y, c_1 v_1}^2 = p_{x/y, c_2 v_2}^2 = 0.069$ a.u. (other $p_{\alpha, c_i v_j}^2 = 0$) correspond to the DFT-PBE level. The multiplicity factor $g_{\boldsymbol{k}_0} = 2$ accounts for K and K' valleys in the BZ. Using Eq. (13), we obtain analytically at room temperature

$$B_{2D}(MoS_2) = 3.1 \times 10^{-5} \text{ cm}^2/\text{s}.$$

This result leads to the intrinsic bimolecular radiative lifetime of

$$\tau_{bm}(MoS_2, n = 10^{11} \text{ cm}^{-2}) \sim 300 \text{ ns}$$

for a charge carrier density of $n = 10^{11}$ cm^{-2}, which serves as a reasonable lower limit, given the constraints expressed in Eq. (A12) and the available experimental data: 10^{10} cm^{-2} [94], $(0.34–2.1) \times 10^{12}$ cm^{-2} [95], $(0.1–2.2) \times 10^{12}$ cm^{-2} [96], and $(4–12) \times 10^{12}$ cm^{-2} [97].

The bimolecular radiative recombination coefficient can be directly evaluated from DFT by approximating the analytical integral in Eq. (10) over the full BZ as a discrete summation over the k points of the 2D irreducible BZ. Using discrete values $f_{\boldsymbol{k}}$ of a generic function $f(\boldsymbol{k})$, the integral can be expressed as follows [[98], Eqs. (4.34), (4.44), and (4.35) therein]

$$(2\pi)^{-d} \int_{BZ} f(\boldsymbol{k}) \, d\boldsymbol{k} \approx \Omega_{cell}^{-1} \sum_{\boldsymbol{k} \in IBZ} w_{\boldsymbol{k}} f_{\boldsymbol{k}}, \qquad (14)$$

where $w_{\boldsymbol{k}} = g_{\boldsymbol{k}}/N_{\boldsymbol{k}}$, with $N_{\boldsymbol{k}}$ representing the number of k points in the full 2D BZ. The weights satisfy the normalization condition $\sum_{\boldsymbol{k} \in IBZ} w_{\boldsymbol{k}} = 1$. In 2D the symbol Ω_{cell} denotes the lateral area of a 2D primitive cell.

The bimolecular radiative recombination coefficient B_{2D} and radiative lifetime $\tau_{bm} = 1/(n B_{2D})$ for materials with the highest optical coupling between band edges are listed in Table II, alongside well-established TMDCs. Both quantities were normalized by the refractive index to facilitate comparison across systems and reduce uncertainties. The radiative coefficients obtained are comparable to those for the optically active MoS_2 monolayer, indicating their potential for practical optical applications. A correlation is observed between high optical coupling at the band edge and optimal values of experimentally accessible quantities, with additional variability attributed to differences in the electronic structure such as a joint density of states [32,39]. Table II shows that the bimolecular radiative lifetime of independent charge carriers is about two orders of magnitude longer than experimental values for MoS_2 at room temperature: 0.58 ns [99] and 0.85 ns [100].

D. Excitonic effects

The results presented above are based on the independent particle approximation within DFT, offering an initial framework for studying optical transitions in 2DMs. While higher-level theories are necessary to accurately capture excitonic effects and electronic screening [[101], chap.20], [[98], chap.21], [102], the high-throughput nature of this study makes solving the BSE for all materials impractical. Consequently, we computed and presented exciton characteristics for a selected subset of materials in Table I. Low-energy exciton eigenvalues are listed side-by-side with corresponding optical couplings obtained at the GW-BSE level. Inspired by the BSE oscillator strength [103–105], the effective BSE momentum matrix element is expressed as a coherent sum of DFT momentum matrix elements in the full BZ weighted by a BSE eigenvector $\mathcal{A}_{v_j c_i, \boldsymbol{k}}^{(\lambda)}$ corresponding to the exciton energy

TABLE II. Bimolecular radiative recombination coefficients and intrinsic radiative lifetimes at room temperature for direct band gap 2DMs with the strongest optical coupling at the band edges. The properties are normalized by the refractive index. B_{2D} and τ_{bm} were computed using DFT with the carrier density of $n = 10^{11}$ cm^{-2} at $T = 300$ K. The exciton radiative lifetime was esimated using Eq. (16) incorporating the $E_{exc}^{(\lambda)}$ and $\langle p_{exc}^2(\lambda) \rangle_\alpha$ characteristics of the brightest exciton states in Table I.

Material structure	$B_{2D}/n_r \times 10^5$ (cm^2/s)	$\tau_{bm} n_r$ (μs)	$\tau_{exc} n_r$ (ns)
GaSeCl	2.9	0.3	0.2
BiTeCl	1.2	0.8	6
Bi$_2$Se$_2$Te	0.44	2.3	16
ZrNCl	1.5	0.7	1
TiNBr	0.49	2.1	6
MoS$_2$	0.41	2.5	3
TiNCl	0.42	2.4	6
MoSeS	0.45	2.2	4
MoSe$_2$	0.57	1.7	4

$E_{\text{exc}}^{(\lambda)}$

$$\langle p_{\text{exc}}^2(\lambda)\rangle_\alpha = \frac{1}{3}\sum_\alpha \left|\sum_{i,j}\sum_{\boldsymbol{k}\in\text{FBZ}} p_{\alpha,v_jc_i,\boldsymbol{k}}\,\mathcal{A}_{v_jc_i,\boldsymbol{k}}^{(\lambda)}\right|^2$$

$$= \frac{m_0^2}{3\hbar^2}\sum_\alpha \left|\sum_{i,j}\sum_{\boldsymbol{k}\in\text{FBZ}} (E_{c_i,\boldsymbol{k}} - E_{v_j,\boldsymbol{k}})\boldsymbol{r}_{\alpha,v_jc_i,\boldsymbol{k}}\,\mathcal{A}_{v_jc_i,\boldsymbol{k}}^{(\lambda)}\right|^2$$

$$\approx \frac{m_0^2 E_g^2}{3\hbar^2}\sum_\alpha \left|\sum_{i,j}\sum_{\boldsymbol{k}\in\text{FBZ}} \boldsymbol{r}_{\alpha,v_jc_i,\boldsymbol{k}}\,\mathcal{A}_{v_jc_i,\boldsymbol{k}}^{(\lambda)}\right|^2.$$
$$(15)$$

Here the band gap E_g must be calculated at the same level of theory as dipole matrix elements $\boldsymbol{r}_{\alpha,vc,\boldsymbol{k}}$ (DFT-PBE in our case). The approximation in the last line of Eq. (15) is justified only for the lowest energy excitons and was verified for MoS$_2$. The term $\sum_\alpha |\sum_{i,j}\sum_{\boldsymbol{k}\in\text{FBZ}} \boldsymbol{r}_{\alpha,v_jc_i,\boldsymbol{k}}\,\mathcal{A}_{v_jc_i,\boldsymbol{k}}^{(\lambda)}|^2$ is referred in VASP documentation as the BSE oscillator strength and stored in vasprun.xml file under the 'opticaltransitions' tag in units of Å^2. Across all materials studied at the BSE level, bright excitons exhibit stronger optical coupling than in the independent-particle approximation (Table I). Mg$_2$Al$_2$Se$_5$ was included in Table I as a benchmark material with inherently weak optical coupling, demonstrating a consistency between the DFT and BSE levels. Characteristics of exciton optical coupling in bulk GaAs are also listed in Table I for comparison with 2DMs. The optical coupling $\langle p_{\text{exc}}^2\rangle_\alpha$ in GaAs exceeds that in 2DMs by less than an order of magnitude. It should be noted that the exciton binding energy in GaAs (60 meV versus 24 meV in Ref. [106] obtained using a denser k-mesh) is much weaker than in 2DMs, where it ranges from 0.2 to 1.4 eV and approximately scales with the quasiparticle band gap as $E_b \approx 0.27 E_g^{\text{GW}}$. This scaling is very close to the empirical ratio of 1/4 reported previously [107,108].

All materials in Table I with a band gap at Γ exhibit doubly degenerate CBE and VBE states. Exciton energies and momentum matrix elements typically lead to either a 3+1 or 2+2 configuration. The 3+1 case, observed in materials such as GaSeCl and TiNCl, consists of three dark excitons and one bright exciton, analogous to triplet and singlet states. In the 2+2 configuration, both excitons can be bright (e.g., BiTeCl) or a mix of bright and dark (e.g., Bi$_2$Se$_2$Te). In many cases, dark and bright excitons are degenerate (e.g., TiNBr, MoS$_2$) or nearly so (e.g., ZrNCl), facilitating efficient radiative recombination. However, in some materials, the bright exciton energy exceeds that of the dark exciton by more than k_BT at room temperature. These materials are expected to exhibit characteristics of both direct and indirect semiconductors—similar to hybrid lead halide perovskites—potentially benefiting photovoltaic applications. In hybrid perovskites, this effect arises from Rashba splitting [92,109] or dynamic disorder [110,111], whereas here it originates from disparities in exciton binding energies. The presence of a dark exciton ground state has been observed in layered lead halide perovskites [112] and in TMDCs such as WS$_2$ and WSe$_2$ [113–115]. In the latter case, the dark exciton ground state arises from spin-forbidden optical transitions due to an inverted spin ordering of the two lowest-energy conduction bands in the K valley as compared to MoS$_2$ [116]. Notably, the bulk parent structure of BiTeCl has been previously identified as nanocrystals hosting a bright exciton ground state [117].

The exciton radiative lifetime can be estimated as the inverse of the Einstein coefficient

$$\tau_{\text{exc}} \approx \left[\frac{n_r q_e^2}{\pi\epsilon_0\hbar^2 m_0^2 c^3}E_{\text{exc}}\langle p_{\text{exc}}^2\rangle_\alpha\right]^{-1}.\qquad(16)$$

Using the values of $E_{\text{exc}}^{(\lambda)}$ and $\langle p_{\text{exc}}^2(\lambda)\rangle_\alpha$ from Table I for one of the bright excitons in MoS$_2$, we obtain $\tau_{\text{exc}} \sim 0.8$ ns, in agreement with experimental data [99,100]. The estimated radiative lifetimes of bright excitons originating from band edges in materials with strong optical coupling are presented in Table II. As with MoS$_2$, these lifetimes fall within the nanosecond range, with an average value of $\tau_{\text{exc}}n_r \sim 5$ ns across materials. These exciton lifetimes are consistently shorter than the bimolecular radiative lifetime of independent charge carriers, suggesting potential advantages for achieving high internal quantum efficiency, provided that nonradiative losses are minimized. These results also indicate promise for the development of optoelectronic devices, such as light-emitting diodes and lasers, where fast radiative recombination is crucial for efficient operation [[33], chap. 7.1.1] and [[118], chap. 14.4.2].

E. Validation and limitations

To benchmark our results for optical transition matrix elements, we selected well-studied materials: bulk GaAs, GaN, and monolayer MoS$_2$. The *velocity* matrix elements are chosen for comparison and presented in Table III for three different exchange-correlation functionals: PBE, HSE06 [75,119], and Yukawa screened hybrid (YSH) [120]. For local functionals, such as PBE, velocity and momentum matrix elements are equivalent to each other [45,90,121,122]. In the case of nonlocal functionals, such as HSE06 and YSH hybrid functionals, the velocity operator contains an additional contribution $\langle\phi_{c,\boldsymbol{k}}|\mathbb{i}[\hat{V}_{\text{nl}},\boldsymbol{r}]|\phi_{v,\boldsymbol{k}}\rangle$ due to the nonlocal nature of the Hartree-Fock potential. This additional contribution to the velocity matrix elements, inherent to hybrid functionals, assures their better agreement with experimental values, which are obtained from the energy parameter E_P derived from empirical band structure measurements. While DFT-PBE underestimates the optical transition strength by approximately 35% compared to both experimental data and hybrid functionals, this discrepancy is systematic. Consequently, trends in the relative efficiency of optical transitions at the band edges, as predicted by DFT-PBE, are expected to remain valid.

The energy parameter E_P is suitable for benchmarking purposes, however, caution is advised when utilizing it for predicting the efficiency of radiative recombination [126]. This parameter accounts for coupling between the conduction band and valence states, including the split-off band ($\Gamma_{\text{so}} \to \Gamma_c$ in GaAs and GaN). However, the split-off band has a negligible contribution to radiative optical transitions at room temperature due to its low thermal occupation. The high excess energy ($\Delta_{\text{so}} > k_BT$) results in a reduced population of carriers in the split-off band at low carrier densities, leading to

TABLE III. Velocity matrix elements $v^2_{x,vc} = \sum_{i,j} v^2_{x,v_j c_i}$ (a.u.) computed at two different levels of theory and compared with experiment. Degeneracy of bands is indicated in brackets.

Material	Transitions	PBE (this work)	Hybrid (HSE06 and YSH)	Experiment
GaAs (bulk)	$\Gamma^{(\times 2)}_{so}, \Gamma^{(\times 4)}_{lh,hh} \rightarrow \Gamma^{(\times 2)}_{c}$	0.62	0.80 [45]	0.83–1.1 [34–37,123]
GaN (bulk, wurtzite)	$\Gamma^{(\times 2)}_{so}, \Gamma^{(\times 2)}_{lh}, \Gamma^{(\times 2)}_{hh} \rightarrow \Gamma^{(\times 2)}_{c}$	0.36	0.49 [45,124]	0.51–0.69 [30,37,125]
MoS$_2$ (monolayer)	$K_{v_1,v_2} \rightarrow K_{c_1,c_2}$	0.14	0.21 [45]	–

an approximately 30% reduction in the effective momentum matrix element $\langle p^2_{vc} \rangle_{\alpha,300\ K}$ relative to the values listed in Table III.

IV. CONCLUSIONS

We conducted a comprehensive benchmarking of optical transition matrix elements in direct band gap 2DMs, including well-studied TMDCs. Using a temperature-dependent summation approach, we ranked materials based on the matrix elements of the lowest-energy transitions that dominate spontaneous emission, accounting for thermal population factors. Our analysis identified transition-metal nitrogen halides (ZrNCl, TiNBr, TiNCl) and bismuth chalcohalides (BiTeCl) with optical coupling at the band edges comparable to or exceeding that of MoS$_2$. Some of these materials exhibit direct band gaps in the visible range, making them promising candidates for optoelectronic applications. However, despite strong in-plane dipole transitions, most 2DMs underperform relative to bulk semiconductors due to a combination of factors, including the absence of out-of-plane optical components, reduced orbital degeneracy at the band edges due to lower crystal symmetry, and spin degeneracy lifting at non-time-reversal-invariant k points.

To better understand interband transitions, we introduced the orbital overlap tensor as a quantitative metric. Our analysis revealed a significant fraction of d-d transitions in TMDCs, which are nominally forbidden by atomic selection rules yet exhibit strong optical coupling that increases with the ionicity of the bond. Conventional explanations based on spin-orbit coupling and crystal field splitting proved insufficient. Instead, we established a correlation between anomalous BECs and interband optical coupling, linking charge redistribution dynamics to optical transition strength. Real-space visualization of optical dipoles confirmed their localization at transition-metal sites in MoS$_2$, ruling out conventional orbital hybridization as the primary factor in optical activity.

We derived an analytical expression for the radiative recombination coefficient in 2DMs, explicitly incorporating multivalley and multiband effects. However, radiative lifetimes computed within the independent-particle approximation were two orders of magnitude longer than experimental values for MoS$_2$. This discrepancy was resolved by including excitonic effects at the GW-BSE level for a selected subset of materials. Notably, we observed a correlation between the effective BSE momentum matrix element and DFT-derived properties, suggesting that preliminary DFT-based screening can significantly reduce computational costs. However, even materials with direct band gaps and strong optical coupling at

the DFT level can exhibit dark excitons as their lowest-energy states, making them quasidirect band gap semiconductors. This phenomenon is analogous to that observed in hybrid lead halide perovskites, but in 2DMs, it is driven by excitonic effects rather than Rashba splitting or dynamic disorder. This insight is critical for engineering excitonic recombination dynamics in next-generation optoelectronic materials.

DATA AVAILABILITY

Some of the data that support the findings of this article are openly available [65]. Data in the plots are not publicly available. The data are available from the authors upon reasonable request.

APPENDIX: ANALYTICAL DERIVATION OF B_{2D}

Here, we present the analytical derivation of the bimolecular recombination coefficient for a 2DM. For simplicity, we

assume there is only one valence band and one conduction band (both nondegenerate) with isotropic band dispersion. The extension of this result to multiple bands with additional splittings in energy is straightforward. We will also neglect any possible variation of the momentum matrix element $\langle p_{vc,k}^2 \rangle_\alpha$ as a function of $\boldsymbol{k}$ in the vicinity of the band extrema $\boldsymbol{k}_0$. By combining Eqs. (10) and (11), we obtain our starting point

$$
B_{2D} = \frac{n_r q_e^2}{\pi \epsilon_0 \hbar^2 m_0^2 c^3} \langle p_{vc,k_0}^2 \rangle_\alpha (2\pi)^{-2} n^{-2} g_{k_0}
$$

$$
\times \int_0^\infty f_{c,k}(1 - f_{v,k})(E_{c,k} - E_{v,k})\, 2\pi k\, dk, \quad \text{(A1)}
$$

where we used $d\boldsymbol{k} \to 2\pi k\, dk$ in a 2D BZ with isotropic band dispersion. The integral is evaluated in the vicinity of the band extremum $\boldsymbol{k}_0$. The factor g_{k_0} represents multiplicity of $\boldsymbol{k}_0$ in the whole BZ. The band dispersion is expressed in terms of effective masses m_c and m_v as follows:

$$
E_{c,k} = E_g + \frac{\hbar^2 k^2}{2m_c} \quad \text{(A2)}
$$

and

$$
E_{v,k} = -\frac{\hbar^2 k^2}{2m_v}. \quad \text{(A3)}
$$

The occupancy of states in the conduction band, in the limit of a low areal density of optical excitations n (the limit will be rigorously defined at the end of this section), can be approximated as

$$
f_{c,k} = \frac{1}{1 + \exp[(E_{c,k} - \mu_c)/k_B T]} \approx e^{(\mu_c - E_{c,k})/k_B T}, \quad \text{(A4)}
$$

and similarly for the valence band as

$$
1 - f_{v,k} = 1 - \frac{1}{1 + \exp[(E_{v,k} - \mu_v)/k_B T]} \approx e^{(E_{v,k} - \mu_v)/k_B T}. \quad \text{(A5)}
$$

The occupancy product in Eq. (A1) becomes

$$
f_{c,k}(1 - f_{v,k}) = e^{(\mu_c - \mu_v)/k_B T}\, e^{(E_{v,k} - E_{c,k})/k_B T}. \quad \text{(A6)}
$$

The quasi Fermi levels μ_c and μ_v can be related to the areal density of optical excitations in the conduction band as

$$
n = (2\pi)^{-2} g_{k_0} \int_0^\infty f_{c,k}\, 2\pi k\, dk
$$

$$
\approx \frac{g_{k_0} m_c k_B T}{2\pi \hbar^2} e^{\mu_c/k_B T} e^{-E_g/k_B T}, \quad \text{(A7)}
$$

and the same density in the valence band is given by

$$
n = (2\pi)^{-2} g_{k_0} \int_0^\infty (1 - f_{v,k})\, 2\pi k\, dk
$$

$$
\approx \frac{g_{k_0} m_v k_B T}{2\pi \hbar^2} e^{-\mu_v/k_B T}. \quad \text{(A8)}
$$

Combining Eqs. (A7) and (A8) results in the exponential term expressed as

$$
e^{(\mu_c - \mu_v)/k_B T} = \frac{(2\pi)^2 \hbar^4 n^2}{g_{k_0}^2 m_c m_v (k_B T)^2} e^{E_g/k_B T}. \quad \text{(A9)}
$$

Note that $e^{(\mu_c - \mu_v)/k_B T} \propto n^2$, which leads to the elimination of the carrier concentration from the final expression for B_{2D} in the limit of a low density of optical excitations. With Eqs. (A6) and (A9), the integral in Eq. (A1) can be evaluated analytically

$$
(2\pi)^{-2} g_{k_0} \int_0^\infty f_{c,k}(1 - f_{v,k})(E_{c,k} - E_{v,k})\, 2\pi k\, dk
$$

$$
\approx (2\pi)^{-1} g_{k_0}\, e^{(\mu_c - \mu_v)/k_B T} \int_0^\infty
$$

$$
\times e^{(E_{v,k} - E_{c,k})/k_B T}(E_{c,k} - E_{v,k})\, k\, dk
$$

$$
= \frac{2\pi \hbar^2 n^2 (E_g + k_B T)}{g_{k_0} k_B T (m_c + m_v)}. \quad \text{(A10)}
$$

After substituting this result back into Eq. (A1) and noting that $E_g \gg k_B T$, we obtain a final expression for the bimolecular recombination coefficient in SI units, in the limit of low density of optical excitations, with material-dependent terms grouped at the end

$$
B_{2D} = \frac{2q_e^2}{c^3 m_0^2 \epsilon_0 k_B T} \frac{n_r E_g \langle p_{vc,k_0}^2 \rangle_\alpha}{g_{k_0}(m_c + m_v)}. \quad \text{(A11)}
$$

The low-density approximation in Eqs. (A7) and (A8) has less than 5% error as long as the areal density of charge carriers satisfies

$$
n \lesssim 0.017\, g_{k_0} k_B T\, \hbar^{-2} \min(m_v, m_c). \quad \text{(A12)}
$$

This expression yields the upper limit of 5×10^{11} cm^{-2} for the low carrier density at room temperature, with $g_{k_0} = 2$ and a mass of $0.43m_0$, which are parameters relevant to MoS$_2$. The expression derived for the 2D bimolecular recombination coefficient [Eq. (A11)] is in agreement with that given by Blood [[60], Appendix B.5] in the context of quantum wells for double-degenerate bands.

For comparison, the spontaneous recombination coefficient (cm^3/s) in bulk materials, in the limit of low carrier density, is

$$
B_{3D} = \frac{2\sqrt{2\pi} q_e^2 \hbar}{c^3 m_0^2 \epsilon_0 (k_B T)^{3/2}} \frac{n_r E_g \langle p_{vc,k_0}^2 \rangle_\alpha}{g_{k_0}(m_c + m_v)^{3/2}}, \quad \text{(A13)}
$$

which is consistent with the expressions quoted earlier by Im et al. [126] and by Landsberg [[131], Eq. (4.5.23)], with the exception of differences in numerical factor of two that accounts for double-degenerate bands. Differences between B_{3D} and B_{2D} are related to the effect of dimensionality on the joint density of states, weighted by the Fermi-Dirac occupation statistics.

[1] K. S. Novoselov, Nobel lecture: Graphene: Materials in the flatland, Rev. Mod. Phys. **83**, 837 (2011).

[2] N. R. Glavin, R. Rao, V. Varshney, E. Bianco, A. Apte, A. Roy, E. Ringe, and P. M. Ajayan, Emerging applications of elemental 2D materials, Adv. Mater. **32**, 1904302 (2020).

[3] S. Z. Butler, S. M. Hollen, L. Cao, Y. Cui, J. A. Gupta, H. R. Gutiérrez, T. F. Heinz, S. S. Hong, J. Huang, A. F. Ismach, E. Johnston-Halperin, M. Kuno, V. V. Plashnitsa, R. D. Robinson, R. S. Ruoff, S. Salahuddin, J. Shan, L. Shi, M. G. Spencer, M. Terrones *et al.*, Progress, challenges, and opportunities in two-dimensional materials beyond graphene, ACS Nano **7**, 2898 (2013).

[4] G. Wang, A. Chernikov, M. M. Glazov, T. F. Heinz, X. Marie, T. Amand, and B. Urbaszek, Colloquium: Excitons in atomically thin transition metal dichalcogenides, Rev. Mod. Phys. **90**, 021001 (2018).

[5] A. Chaves, J. G. Azadani, H. Alsalman, D. R. da Costa, R. Frisenda, A. J. Chaves, S. H. Song, Y. D. Kim, D. He, J. Zhou, A. Castellanos-Gomez, F. M. Peeters, Z. Liu, C. L. Hinkle, S.-H. Oh, P. D. Ye, S. J. Koester, Y. H. Lee, P. Avouris, X. Wang *et al.*, Bandgap engineering of two-dimensional semiconductor materials, npj 2D Mater. Appl. **4**, 29 (2020).

[6] A. Ramasubramaniam, Large excitonic effects in monolayers of molybdenum and tungsten dichalcogenides, Phys. Rev. B **86**, 115409 (2012).

[7] H. R. Gutiérrez, N. Perea-López, A. L. Elías, A. Berkdemir, B. Wang, R. Lv, F. López-Urías, V. H. Crespi, H. Terrones, and M. Terrones, Extraordinary room-temperature photoluminescence in triangular WS$_2$ monolayers, Nano Lett. **13**, 3447 (2013).

[8] D. K. Sang, B. Wen, S. Gao, Y. Zeng, F. Meng, Z. Guo, and H. Zhang, Electronic and optical properties of two-dimensional tellurene: From first-principles calculations, Nanomaterials **9**, 1075 (2019).

[9] M. Buscema, D. J. Groenendijk, S. I. Blanter, G. A. Steele, H. S. J. van der Zant, and A. Castellanos-Gomez, Fast and broadband photoresponse of few-layer black phosphorus field-effect transistors, Nano Lett. **14**, 3347 (2014).

[10] V. Tran, R. Soklaski, Y. Liang, and L. Yang, Layer-controlled band gap and anisotropic excitons in few-layer black phosphorus, Phys. Rev. B **89**, 235319 (2014).

[11] X. Wang, A. M. Jones, K. L. Seyler, V. Tran, Y. Jia, H. Zhao, H. Wang, L. Yang, X. Xu, and F. Xia, Highly anisotropic and robust excitons in monolayer black phosphorus, Nat. Nanotechnol. **10**, 517 (2015).

[12] K. F. Mak, C. Lee, J. Hone, J. Shan, and T. F. Heinz, Atomically thin MoS$_2$: A new direct-gap semiconductor, Phys. Rev. Lett. **105**, 136805 (2010).

[13] K. F. Mak, K. He, J. Shan, and T. F. Heinz, Control of valley polarization in monolayer MoS$_2$ by optical helicity, Nat. Nanotechnol. **7**, 494 (2012).

[14] D. Y. Qiu, F. H. da Jornada, and S. G. Louie, Optical spectrum of MoS$_2$: Many-body effects and diversity of exciton states, Phys. Rev. Lett. **111**, 216805 (2013).

[15] G. Sallen, L. Bouet, X. Marie, G. Wang, C. R. Zhu, W. P. Han, Y. Lu, P. H. Tan, T. Amand, B. L. Liu, and B. Urbaszek, Robust optical emission polarization in MoS$_2$ monolayers through selective valley excitation, Phys. Rev. B **86**, 081301(R) (2012).

[16] A. Splendiani, L. Sun, Y. Zhang, T. Li, J. Kim, C.-Y. Chim, G. Galli, and F. Wang, Emerging photoluminescence in monolayer MoS$_2$, Nano Lett. **10**, 1271 (2010).

[17] A. K. M. Newaz, D. Prasai, J. I. Ziegler, D. Caudel, S. Robinson, R. F. Haglund, Jr., and K. I. Bolotin, Electrical control of optical properties of monolayer MoS$_2$, Solid State Commun. **155**, 49 (2013).

[18] T. Cao, G. Wang, W. Han, H. Ye, C. Zhu, J. Shi, Q. Niu, P. Tan, E. Wang, B. Liu, and J. Feng, Valley-selective circular dichroism of monolayer molybdenum disulphide, Nat. Commun. **3**, 887 (2012).

[19] H. Zeng, J. Dai, W. Yao, D. Xiao, and X. Cui, Valley polarization in MoS$_2$ monolayers by optical pumping, Nat. Nanotechnol. **7**, 490 (2012).

[20] G. Wang, Y. Zhang, C. You, B. Liu, Y. Yang, H. Li, A. Cui, D. Liu, and H. Yan, Two dimensional materials based photodetectors, Infrared Phys. Technol. **88**, 149 (2018).

[21] F. Wang, Z. Wang, L. Yin, R. Cheng, J. Wang, Y. Wen, T. A. Shifa, F. Wang, Y. Zhang, X. Zhan, and J. He, 2D library beyond graphene and transition metal dichalcogenides: a focus on photodetection, Chem. Soc. Rev. **47**, 6296 (2018).

[22] M. Gao, L. Yu, Q. Lv, F. Kang, Z.-H. Huang, and R. Lv, Photoluminescence manipulation in two-dimensional transition metal dichalcogenides, J. Mater. **9**, 768 (2023).

[23] Y. Li, H. Sun, L. Gan, J. Zhang, J. Feng, D. Zhang, and C.-Z. Ning, Optical properties and light-emission device applications of 2-D layered semiconductors, Proc. IEEE **108**, 676 (2020).

[24] K. Xie, X. Li, and T. Cao, Theory and ab initio calculation of optically excited states—recent advances in 2D materials, Adv. Mater. **33**, 1904306 (2021).

[25] H. Zhao, Q. Guo, F. Xia, and H. Wang, Two-dimensional materials for nanophotonics application, Nanophotonics **4**, 128 (2015).

[26] M. Bernardi, C. Ataca, M. Palummo, and J. C. Grossman, Optical and electronic properties of two-dimensional layered materials, Nanophotonics **6**, 479 (2017).

[27] M. Fox, *Optical Properties of Solids*, 2nd ed. (Oxford University Press, Oxford, England, 2010).

[28] M. L. Cohen and S. G. Louie, *Fundamentals of Condensed Matter Physics* (Cambridge University Press, Cambridge, England, 2019).

[29] M. S. Masakatsu Suzuki and T. U. Takeshi Uenoyama, Theoretical study of momentum matrix elements of GaN, Jpn. J. Appl. Phys. **35**, 543 (1996).

[30] S. Shokhovets, G. Gobsch, and O. Ambacher, Momentum matrix element and conduction band nonparabolicity in wurtzite GaN, Appl. Phys. Lett. **86**, 161908 (2005).

[31] S. H. Rhim, M. Kim, A. J. Freeman, and R. Asahi, Fully first-principles screened-exchange LDA calculations of excited states and optical properties of III-V semiconductors, Phys. Rev. B **71**, 045202 (2005).

[32] M. Kato, M. Nishiwaki, and H. Fujiwara, Very high oscillator strength in the band-edge light absorption of zincblende, chalcopyrite, kesterite, and hybrid perovskite solar cell materials, Phys. Rev. Mater. **4**, 035402 (2020).

[33] P. Yu and M. Cardona, *Fundamentals of Semiconductors: Physics and Materials Properties* (Springer, Berlin, Germany, 2010).

[34] C. Hermann and C. Weisbuch, k·p perturbation theory in III-V compounds and alloys: a reexamination, Phys. Rev. B **15**, 823 (1977).

[35] P. Pfeffer and W. Zawadzki, Five-level k·p model for the conduction and valence bands of GaAs and InP, Phys. Rev. B **53**, 12813 (1996).

[36] M. Cardona, N. E. Christensen, and G. Fasol, Relativistic band structure and spin-orbit splitting of zinc-blende-type semiconductors, Phys. Rev. B **38**, 1806 (1988).

[37] I. Vurgaftman, J. R. Meyer, and L. R. Ram-Mohan, Band parameters for III-V compound semiconductors and their alloys, J. Appl. Phys. **89**, 5815 (2001).

[38] T. Ketolainen, N. Macháčová, and F. Karlický, Optical gaps and excitonic properties of 2D materials by hybrid time-dependent density functional theory: Evidences for monolayers and prospects for van der Waals heterostructures, J. Chem. Theory Comput. **16**, 5876 (2020).

[39] S. Gupta, S. N. Shirodkar, A. Kutana, and B. I. Yakobson, In pursuit of 2D materials for maximum optical response, ACS Nano **12**, 10880 (2018).

[40] M. Bernardi, M. Palummo, and J. C. Grossman, Extraordinary sunlight absorption and one nanometer thick photovoltaics using two-dimensional monolayer materials, Nano Lett. **13**, 3664 (2013).

[41] A. Kumar and P. K. Ahluwalia, A first principle comparative study of electronic and optical properties of $1H-MoS_2$ and $2H-MoS_2$, Mater. Chem. Phys. **135**, 755 (2012).

[42] S. Haastrup, M. Strange, M. Pandey, T. Deilmann, P. S. Schmidt, N. F. Hinsche, M. N. Gjerding, D. Torelli, P. M. Larsen, A. C. Riis-Jensen, J. Gath, K. W. Jacobsen, J. Jørgen Mortensen, T. Olsen, and K. S. Thygesen, The computational 2D materials database: high-throughput modeling and discovery of atomically thin crystals, 2D Mater. **5**, 042002 (2018).

[43] H. Gu, Z. Guo, L. Huang, M. Fang, and S. Liu, Investigations of optical functions and optical transitions of 2D semiconductors by spectroscopic ellipsometry and DFT, Nanomaterials **13**, 196 (2023).

[44] M. H. Jameel, M. S. B. Roslan, M. Z. H. B. Mayzan, I. A. Shaaban, S. Z. H. Rizvi, M. A. B. Agam, S. Saleem, and M. A. Assiri, A comparative DFT study of bandgap engineering and tuning of structural, electronic, and optical properties of 2D WS_2, PtS_2, and MoS_2 between WSe_2, $PtSe_2$, and $MoSe_2$ materials for photocatalytic and solar cell applications, J. Inorg. Organomet. Polym. Mater. **34**, 322 (2024).

[45] O. Rubel and P. Blaha, Length-gauge optical matrix elements in WIEN2k, Computation **10**, 22 (2022).

[46] P. Hohenberg and W. Kohn, Inhomogeneous electron gas, Phys. Rev. **136**, B864 (1964).

[47] W. Kohn and L. J. Sham, Self-consistent equations including exchange and correlation effects, Phys. Rev. **140**, A1133 (1965).

[48] M. N. Gjerding, A. Taghizadeh, A. Rasmussen, S. Ali, F. Bertoldo, T. Deilmann, N. R. Knøsgaard, M. Kruse, A. H. Larsen, S. Manti, T. G. Pedersen, U. Petralanda, T. Skovhus, M. K. Svendsen, J. J. Mortensen, T. Olsen, and K. S. Thygesen, Recent progress of the computational 2D materials database (C2DB), 2D Mater. **8**, 044002 (2021).

[49] N. A. Pike, B. Van Troeye, A. Dewandre, G. Petretto, X. Gonze, G.-M. Rignanese, and M. J. Verstraete, Origin of the counterintuitive dynamic charge in the transition metal dichalcogenides, Phys. Rev. B **95**, 201106(R) (2017).

[50] A. Jain, S. P. Ong, G. Hautier, W. Chen, W. D. Richards, S. Dacek, S. Cholia, D. Gunter, D. Skinner, G. Ceder, and K. A. Persson, Commentary: The Materials Project: A materials genome approach to accelerating materials innovation, APL Mater. **1**, 011002 (2013).

[51] S. P. Ong, L. Wang, B. Kang, and G. Ceder, Li-Fe-P-O_2 phase diagram from first principles calculations, Chem. Mater. **20**, 1798 (2008).

[52] G. Kresse and J. Hafner, *Ab initio* molecular dynamics for liquid metals, Phys. Rev. B **47**, 558 (1993).

[53] G. Kresse and J. Furthmüller, Efficiency of *ab-initio* total energy calculations for metals and semiconductors using a plane-wave basis set, Comput. Mater. Sci. **6**, 15 (1996).

[54] P. E. Blöchl, Projector augmented-wave method, Phys. Rev. B **50**, 17953 (1994).

[55] J. P. Perdew, K. Burke, and M. Ernzerhof, Generalized gradient approximation made simple, Phys. Rev. Lett. **77**, 3865 (1996).

[56] G. Kresse and D. Joubert, From ultrasoft pseudopotentials to the projector augmented-wave method, Phys. Rev. B **59**, 1758 (1999).

[57] See Supplemental Material at http://link.aps.org/supplemental/10.1103/PhysRevB.111.195426 for the pseudopotential details, convergence tests and Bader charges calculation details and which includes Refs. [42,48,127–130].

[58] S. Steiner, S. Khmelevskyi, M. Marsmann, and G. Kresse, Calculation of the magnetic anisotropy with projected-augmented-wave methodology and the case study of disordered $Fe_{1-x}CO_x$, Phys. Rev. B **93**, 224425 (2016).

[59] M. Laurien and O. Rubel, Benchmarking exchange-correlation potentials with the mstar60 dataset: Importance of the nonlocal exchange potential for effective mass calculations in semiconductors, Phys. Rev. B **106**, 045204 (2022).

[60] P. Blood, *Quantum Confined Laser Devices: Optical Gain and Recombination in Semiconductors*, 1st ed. (Oxford University Press, Oxford, England, 2015).

[61] M. Schüler, O. E. Peil, G. J. Kraberger, R. Pordzik, M. Marsman, G. Kresse, T. O. Wehling, and M. Aichhorn, Charge self-consistent many-body corrections using optimized projected localized orbitals, J. Phys.: Condens. Matter **30**, 475901 (2018).

[62] V. Wang, N. Xu, J.-C. Liu, G. Tang, and W.-T. Geng, VASP-KIT: A user-friendly interface facilitating high-throughput computing and analysis using VASP code, Comput. Phys. Commun. **267**, 108033 (2021).

[63] S. Xu, Z. Liu, X. Xu, Y. Guo, S.-H. Wei, and X. Zhang, PyArc: A python package for computing absorption and radiative coefficients from first principles, Comput. Phys. Commun. **305**, 109352 (2024).

[64] T. Sander, E. Maggio, and G. Kresse, Beyond the Tamm-Dancoff approximation for extended systems using exact diagonalization, Phys. Rev. B **92**, 045209 (2015).

[65] Files necessary to reproduce this work are available at 10.5281/zenodo.13773214. VASP version 6.4.0 was used except for GW-BSE calculations where VASP 6.5.0 was used. In addition, the archive includes a CSV file summarizing key results for the top-performing direct band gap monolayer materials. The file contains the polarization-averaged momentum

matrix elements at 300 K see Eq. (3), along with information such as k-point coordinates, PBE+SOC band gaps, space group, energy above the convex hull, and database identifiers (DOI, COD, and C2DB).

[66] D. Kaplan, Y. Gong, K. Mills, V. Swaminathan, P. M. Ajayan, S. Shirodkar, and E. Kaxiras, Excitation intensity dependence of photoluminescence from monolayers of MoS$_2$ and WS$_2$/MoS$_2$ heterostructures, 2D Mater. **3**, 015005 (2016).

[67] R. Kappera, D. Voiry, S. E. Yalcin, B. Branch, G. Gupta, A. D. Mohite, and M. Chhowalla, Phase-engineered low-resistance contacts for ultrathin MoS$_2$ transistors, Nat. Mater. **13**, 1128 (2014).

[68] O. Lopez-Sanchez, D. Lembke, M. Kayci, A. Radenovic, and A. Kis, Ultrasensitive photodetectors based on monolayer MoS$_2$, Nat. Nanotechnol. **8**, 497 (2013).

[69] A.-Y. Lu, H. Zhu, J. Xiao, C.-P. Chuu, Y. Han, M.-H. Chiu, C.-C. Cheng, C.-W. Yang, K.-H. Wei, Y. Yang, Y. Wang, D. Sokaras, D. Nordlund, P. Yang, D. A. Muller, M.-Y. Chou, X. Zhang, and L.-J. Li, Janus monolayers of transition metal dichalcogenides, Nat. Nanotechnol. **12**, 744 (2017).

[70] P. Tonndorf, R. Schmidt, P. Böttger, X. Zhang, J. Börner, A. Liebig, M. Albrecht, C. Kloc, O. Gordan, D. R. T. Zahn, S. M. de Vasconcellos, and R. Bratschitsch, Photoluminescence emission and Raman response of monolayer MoS$_2$, MoSe$_2$, and WSe$_2$, Opt. Express **21**, 4908 (2013).

[71] Y. Wang, J. Xiao, H. Zhu, Y. Li, Y. Alsaid, K. Y. Fong, Y. Zhou, S. Wang, W. Shi, Y. Wang, A. Zettl, E. J. Reed, and X. Zhang, Structural phase transition in monolayer MoTe$_2$ driven by electrostatic doping, Nature (London) **550**, 487 (2017).

[72] S. Tongay, H. Sahin, C. Ko, A. Luce, W. Fan, K. Liu, J. Zhou, Y.-S. Huang, C.-H. Ho, J. Yan, D. F. Ogletree, S. Aloni, J. Ji, S. Li, J. Li, F. M. Peeters, and J. Wu, Monolayer behaviour in bulk ReS$_2$ due to electronic and vibrational decoupling, Nat. Commun. **5**, 3252 (2014).

[73] M. Okada, T. Sawazaki, K. Watanabe, T. Taniguch, H. Hibino, H. Shinohara, and R. Kitaura, Direct chemical vapor deposition growth of WS$_2$ atomic layers on hexagonal boron nitride, ACS Nano **8**, 8273 (2014).

[74] R. Kniep, A. Wilms, and H. J. Beister, Phase relations in Ga$_2$X$_3$-GaY$_3$ systems (X=Se, Te; Y=Cl, Br, I) — Crystal growth, structural relations and optical absorption of intermediate compounds GaXY, Mater. Res. Bull. **18**, 615 (1983).

[75] A. V. Krukau, O. A. Vydrov, A. F. Izmaylov, and G. E. Scuseria, Influence of the exchange screening parameter on the performance of screened hybrid functionals, J. Chem. Phys. **125**, 224106 (2006).

[76] A. Vaitkus, A. Merkys, T. Sander, M. Quirós, P. A. Thiessen, E. E. Bolton, and S. Gražulis, A workflow for deriving chemical entities from crystallographic data and its application to the Crystallography Open Database, J. Cheminf. **15**, 123 (2023).

[77] Z. Y. Zhu, Y. C. Cheng, and U. Schwingenschlögl, Giant spin-orbit-induced spin splitting in two-dimensional transition-metal dichalcogenide semiconductors, Phys. Rev. B **84**, 153402 (2011).

[78] T. Cheiwchanchamnangij and W. R. L. Lambrecht, Quasiparticle band structure calculation of monolayer, bilayer, and bulk MoS$_2$, Phys. Rev. B **85**, 205302 (2012).

[79] R. Woods-Robinson, Y. Xiong, J.-X. Shen, N. Winner, M. K. Horton, M. Asta, A. M. Ganose, G. Hautier, and K. A. Persson, Designing transparent conductors using forbidden optical transitions, Matter **6**, 3021 (2023).

[80] M. Fox, Quantum optics: An introduction, *Oxford Master Series in Physics* (Oxford University Press, Oxford, England, 2006).

[81] D. Xiao, G.-B. Liu, W. Feng, X. Xu, and W. Yao, Coupled spin and valley physics in monolayers of MoS$_2$ and other group-VI dichalcogenides, Phys. Rev. Lett. **108**, 196802 (2012).

[82] A. Kormányos, G. Burkard, M. Gmitra, J. Fabian, V. Zólyomi, N. D. Drummond, and V. Fal'ko, K·p theory for two-dimensional transition metal dichalcogenide semiconductors, 2D Mater. **2**, 022001 (2015).

[83] R. Huisman, R. de Jonge, C. Haas, and F. Jellinek, Trigonal-prismatic coordination in solid compounds of transition metals, J. Solid State Chem. **3**, 56 (1971).

[84] S. Maier, S. Steinberg, Y. Cheng, C.-F. Schön, M. Schumacher, R. Mazzarello, P. Golub, R. Nelson, O. Cojocaru-Mirédin, J.-Y. Raty, and M. Wuttig, Discovering electron-transfer-driven changes in chemical bonding in lead chalcogenides (PbX, where X = Te, Se, S, O), Adv. Mater. **32**, 2005533 (2020).

[85] M. Wuttig, C.-F. Schön, M. Schumacher, J. Robertson, P. Golub, E. Bousquet, C. Gatti, and J.-Y. Raty, Halide perovskites: Advanced photovoltaic materials empowered by a unique bonding mechanism, Adv. Funct. Mater. **32**, 2110166 (2022).

[86] C.-F. Schön, S. van Bergerem, C. Mattes, A. Yadav, M. Grohe, L. Kobbelt, and M. Wuttig, Classification of properties and their relation to chemical bonding: Essential steps toward the inverse design of functional materials, Sci. Adv. **8**, eade0828 (2022).

[87] W. Wełnic, S. Botti, L. Reining, and M. Wuttig, Origin of the optical contrast in phase-change materials, Phys. Rev. Lett. **98**, 236403 (2007).

[88] X. Gonze and C. Lee, Dynamical matrices, born effective charges, dielectric permittivity tensors, and interatomic force constants from density-functional perturbation theory, Phys. Rev. B **55**, 10355 (1997).

[89] P. Ghosez, J.-P. Michenaud, and X. Gonze, Dynamical atomic charges: The case of ABO$_3$ compounds, Phys. Rev. B **58**, 6224 (1998).

[90] A. F. Starace, Length and velocity formulas in approximate oscillator-strength calculations, Phys. Rev. A **3**, 1242 (1971).

[91] M. Rohlfing and S. G. Louie, Electron-hole excitations and optical spectra from first principles, Phys. Rev. B **62**, 4927 (2000).

[92] P. Azarhoosh, S. McKechnie, J. M. Frost, A. Walsh, and M. van Schilfgaarde, Research update: Relativistic origin of slow electron-hole recombination in hybrid halide perovskite solar cells, APL Mater. **4**, 091501 (2016).

[93] G. A. Ermolaev, D. V. Grudinin, Y. V. Stebunov, K. V. Voronin, V. G. Kravets, J. Duan, A. B. Mazitov, G. I. Tselikov, A. Bylinkin, D. I. Yakubovsky, S. M. Novikov, D. G. Baranov, A. Y. Nikitin, I. A. Kruglov, T. Shegai, P. Alonso-González, A. N. Grigorenko, A. V. Arsenin, K. S. Novoselov, and V. S. Volkov, Giant optical anisotropy in transition metal

dichalcogenides for next-generation photonics, Nat. Commun. **12**, 854 (2021).

[94] C.-C. Wu, D. Jariwala, V. K. Sangwan, T. J. Marks, M. C. Hersam, and L. J. Lauhon, Elucidating the photoresponse of ultrathin MoS_2 field-effect transistors by scanning photocurrent microscopy, J. Phys. Chem. Lett. **4**, 2508 (2013).

[95] A. R. Myers, D. B. Sulas-Kern, R. Fei, D. Ghoshal, M. A. Hermosilla-Palacios, and J. L. Blackburn, Quantifying carrier density in monolayer MoS_2 by optical spectroscopy, J. Chem. Phys. **161**, 044706 (2024).

[96] H. Qiu, T. Xu, Z. Wang, W. Ren, H. Nan, Z. Ni, Q. Chen, S. Yuan, F. Miao, F. Song, G. Long, Y. Shi, L. Sun, J. Wang, and X. Wang, Hopping transport through defect-induced localized states in molybdenum disulphide, Nat. Commun. **4**, 2642 (2013).

[97] X. Cui, G.-H. Lee, Y. D. Kim, G. Arefe, P. Y. Huang, C.-H. Lee, D. A. Chenet, X. Zhang, L. Wang, F. Ye, F. Pizzocchero, B. S. Jessen, K. Watanabe, T. Taniguchi, D. A. Muller, T. Low, P. Kim, and J. Hone, Multi-terminal transport measurements of MoS_2 using a van der waals heterostructure device platform, Nat. Nanotechnol. **10**, 534 (2015).

[98] R. Martin, *Electronic Structure: Basic Theory and Practical Methods*, 2nd ed. (Cambridge University Press, Cambridge, England, 2020).

[99] A. J. Goodman, A. P. Willard, and W. A. Tisdale, Exciton trapping is responsible for the long apparent lifetime in acid-treated MoS_2, Phys. Rev. B **96**, 121404 (2017).

[100] H. Shi, R. Yan, S. Bertolazzi, J. Brivio, B. Gao, A. Kis, D. Jena, H. G. Xing, and L. Huang, Exciton dynamics in suspended monolayer and few-layer MoS_2 2D crystals, ACS Nano **7**, 1072 (2013).

[101] F. Bechstedt, *Many-Body Approach to Electronic Excitations: Concepts and Applications* (Springer, Berlin, Germany, 2016).

[102] G. Onida, L. Reining, and A. Rubio, Electronic excitations: density-functional versus many-body Green's-function approaches, Rev. Mod. Phys. **74**, 601 (2002).

[103] S. Albrecht, L. Reining, R. Del Sole, and G. Onida, *Ab initio* calculation of excitonic effects in the optical spectra of semiconductors, Phys. Rev. Lett. **80**, 4510 (1998).

[104] W. G. Schmidt, S. Glutsch, P. H. Hahn, and F. Bechstedt, Efficient $\mathcal{O}(n^2)$ method to solve the Bethe-Salpeter equation, Phys. Rev. B **67**, 085307 (2003).

[105] F. Fuchs, C. Rödl, A. Schleife, and F. Bechstedt, Efficient $\mathcal{O}(N^2)$ approach to solve the Bethe-Salpeter equation for excitonic bound states, Phys. Rev. B **78**, 085103 (2008).

[106] J. Sun, J. Yang, and C. A. Ullrich, Low-cost alternatives to the Bethe-Salpeter equation: Towards simple hybrid functionals for excitonic effects in solids, Phys. Rev. Res. **2**, 013091 (2020).

[107] Z. Jiang, Z. Liu, Y. Li, and W. Duan, Scaling universality between band gap and exciton binding energy of two-dimensional semiconductors, Phys. Rev. Lett. **118**, 266401 (2017).

[108] H. Yu, M. Laurien, Z. Hu, and O. Rubel, Exploration of the bright and dark exciton landscape and fine structure of MoS_2 using G_0W_0-BSE, Phys. Rev. B **100**, 125413 (2019).

[109] C. Katan, L. Pedesseau, M. Kepenekian, A. Rolland, and J. Even, Interplay of spin-orbit coupling and lattice distortion in metal substituted 3D tri-chloride hybrid perovskites, J. Mater. Chem. A **3**, 9232 (2015).

[110] C. Zheng, S. Yu, and O. Rubel, Structural dynamics in hybrid halide perovskites: bulk Rashba splitting, spin texture, and carrier localization, Phys. Rev. Mater. **2**, 114604 (2018).

[111] K. T. Munson, E. R. Kennehan, G. S. Doucette, and J. B. Asbury, Dynamic disorder dominates delocalization, transport, and recombination in halide perovskites, Chem **4**, 2826 (2018).

[112] C. Quarti, G. Giorgi, C. Katan, J. Even, and M. Palummo, Exciton ground state fine structure and excited states landscape in layered halide perovskites from combined BSE simulations and symmetry analysis, Adv. Opt. Mater. **12**, 2202801 (2024).

[113] G. Wang, C. Robert, A. Suslu, B. Chen, S. Yang, S. Alamdari, I. C. Gerber, T. Amand, X. Marie, S. Tongay, and B. Urbaszek, Spin-orbit engineering in transition metal dichalcogenide alloy monolayers, Nat. Commun. **6**, 10110 (2015).

[114] A. Arora, M. Koperski, K. Nogajewski, J. Marcus, C. Faugeras, and M. Potemski, Excitonic resonances in thin films of WSe_2: from monolayer to bulk material, Nanoscale **7**, 10421 (2015).

[115] F. Withers, O. Del Pozo-Zamudio, S. Schwarz, S. Dufferwiel, P. M. Walker, T. Godde, A. P. Rooney, A. Gholinia, C. R. Woods, P. Blake, S. J. Haigh, K. Watanabe, T. Taniguchi, I. L. Aleiner, A. K. Geim, V. I. Fal'ko, A. I. Tartakovskii, and K. S. Novoselov, WSe_2 light-emitting tunneling transistors with enhanced brightness at room temperature, Nano Lett. **15**, 8223 (2015).

[116] J. P. Echeverry, B. Urbaszek, T. Amand, X. Marie, and I. C. Gerber, Splitting between bright and dark excitons in transition metal dichalcogenide monolayers, Phys. Rev. B **93**, 121107 (2016).

[117] M. W. Swift, P. C. Sercel, A. L. Efros, J. L. Lyons, and D. J. Norris, Identification of semiconductor nanocrystals with bright ground-state excitons, ACS Nano **18**, 19561 (2024).

[118] D. A. Neamen, *Semiconductor Physics and Devices: Basic Principles*, 3rd ed. (McGraw Hill Higher Education, New York, 2002).

[119] J. Heyd, G. E. Scuseria, and M. Ernzerhof, Hybrid functionals based on a screened Coulomb potential, J. Chem. Phys. **118**, 8207 (2003).

[120] F. Tran and P. Blaha, Implementation of screened hybrid functionals based on the Yukawa potential within the LAPW basis set, Phys. Rev. B **83**, 235118 (2011).

[121] B. Adolph, V. I. Gavrilenko, K. Tenelsen, F. Bechstedt, and R. Del Sole, Nonlocality and many-body effects in the optical properties of semiconductors, Phys. Rev. B **53**, 9797 (1996).

[122] M. Cohen and R. P. McEachran, Length and velocity formulae in approximate oscillator strength calculations, Chem. Phys. Lett. **14**, 201 (1972).

[123] D. E. Aspnes, GaAs lower conduction-band minima: Ordering and properties, Phys. Rev. B **14**, 5331 (1976).

[124] L. C. de Carvalho, A. Schleife, and F. Bechstedt, Influence of exchange and correlation on structural and electronic properties of AlN, GaN, and InN polytypes, Phys. Rev. B **84**, 195105 (2011).

[125] S. Shokhovets, O. Ambacher, B. K. Meyer, and G. Gobsch, Anisotropy of the momentum matrix element, dichroism, and conduction-band dispersion relation of wurtzite semiconductors, Phys. Rev. B **78**, 079902(E) (2008).

[126] J. S. Im, A. Moritz, F. Steuber, V. Härle, F. Scholz, and A. Hangleiter, Radiative carrier lifetime, momentum matrix element, and hole effective mass in GaN, Appl. Phys. Lett. **70**, 631 (1997).

[127] M. Yu and D. R. Trinkle, Accurate and efficient algorithm for Bader charge integration, J. Chem. Phys. **134**, 064111 (2011).

[128] G. Henkelman, A. Arnaldsson, and H. Jónsson, A fast and robust algorithm for bader decomposition of charge density, Comput. Mater. Sci. **36**, 354 (2006).

[129] W. Tang, E. Sanville, and G. Henkelman, A grid-based Bader analysis algorithm without lattice bias, J. Phys.: Condens. Matter **21**, 084204 (2009).

[130] E. Sanville, S. D. Kenny, R. Smith, and G. Henkelman, Improved grid-based algorithm for Bader charge allocation, J. Comput. Chem. **28**, 899 (2007).

[131] P. T. Landsberg, *Recombination in Semiconductors* (Cambridge University Press, Cambridge, England, 1991).